JOURNAL OF AIRCRAFT
Vol. 30, No. 4, July–Aug. 1993

Navier-Stokes Analysis of Three-Dimensional S-Ducts

G. J. Harloff,* C. F. Smith,† J. E. Bruns,‡ and J. R. DeBonis‡
Sverdrup Technology, Inc., Brook Park, Ohio 44142

Full three-dimensional Navier-Stokes computational results are presented for compressible flows within nondiffusing and diffusing S-ducts. The present study provides an understanding of the performance characteristics of typical S-ducts with attached and separated flows, and provides a frame of reference for future computational fluid dynamic studies of internal flows with strong secondary flows. The predicted results, which were obtained using both H- and O-grids, are compared with the experimental wall pressures, static and total pressure fields, and velocity vectors. In addition, computed boundary-layer thickness, velocity profiles in wall coordinates, and skin friction values are presented. The inviscid contributions to the secondary flows are quantified. The S-duct entrance Mach number was 0.6, and the Reynolds number was 1.76 × 10⁶ based on the upstream duct diameter.

Nomenclature

A = sublayer thickness
A^+ = AU_t/ν
C_f = skin friction coefficient
C_{ps} = static pressure coefficient, $(P_{s,\text{local}} - P_{s,\text{ref}})/Q_{\text{ref}}$
C_{pt} = total pressure coefficient, $(P_{t,\text{local}} - P_{s,\text{ref}})/Q_{\text{ref}}$
D = diameter
k = turbulent kinetic energy
P_s = static pressure
P_t = total pressure
Q = dynamic pressure
Re = Reynolds number, $u_{\text{ref}}D/\nu_{\text{ref}}$
S = arc length along centerline of duct
T_w = wall shear stress
U_e = edge velocity
U_t = friction velocity, $\sqrt{T_w/\rho_w}$
U^+ = U/U_t
u = velocity in x direction
v = velocity in y direction
w = velocity in z direction
x = coordinate distance
Y^+ = yU_t/ν
y = coordinate distance
z = coordinate distance
δ = boundary-layer thickness
ε = dissipation
ν = kinematic viscosity
ρ = density
ϕ = circumferential angular position around duct

Subscripts
l = laminar
ref = reference station (station 1)
t = turbulent
w = wall

Introduction

MANY aircraft employ bending rectangular and circular duct geometries in the inlet and exhaust of the propulsion systems. Examples of aircraft with inlet S-ducts include the Boeing 727, Lockheed Tristar (L-1011), General Dynamics F-16, and McDonnell-Douglas F-18. The performance of these types of ducts, which may have strong secondary flows, is usually determined by wind-tunnel testing. Recently, computational fluid dynamic (CFD) capabilities have improved, and both parabolized and full Navier-Stokes (FNS) computer programs are used to predict the flows in these ducts. The purpose of the present study is to apply a FNS computer program, the PARC3D code, to representative three-dimensional duct geometries with secondary flows. The full, three-dimensional Navier-Stokes equations have been closed using an algebraic turbulence model. The entrance velocity and pressure field are permitted to adjust to the duct geometry and the flow losses. Solutions are obtained for H- and O-grids in order to examine the grid effects on the solution. The inviscid contributions to the secondary flowfield are quantified by solving the Euler equations for irrotational and rotational inflow in two S-ducts. This study provides an understanding of the performance characteristics of nondiffusing and diffusing S-ducts and bench marks the PARC3D code.

Recent literature is reviewed to determine the status of experimental data and the state of the art in modeling these kinds of flows. Recommendations are made for further work in the modeling of these ducts.

Previous Studies

Experimental

Bansod and Bradshaw[1] conducted experiments using three constant area S-ducts. The flow was incompressible with a Reynolds number of 0.5 × 10⁶, based on diameter. Willmer et al.[2] tested a circular inlet and a S-duct at Mach numbers from 0 to 0.21, and at incidence and sideslip angles from 0 to 40 deg. Guo and Seddon[3] experimentally investigated the incompressible flow in a constant area, rectangular S-duct mounted in a wind tunnel. The duct had two 35-deg bends, and tests were conducted to a 30-deg angle of attack and to a 10-deg angle of yaw. The Reynolds number, based on hydraulic diameter, varied between 2.1 × 10⁵ and 2.7 × 10⁵. Total pressure contours, recovery, and turbulence levels were reported. Flow separation, large exit-flow distortion, a pair of counter-rotating vortices, and high-turbulence levels were observed. McMillan[4] tested a diffusing duct to obtain incompressible CFD validation data and observed that a pair of counter-rotating streamwise vortices dominated the flow. Schmidt et al.[5] conducted experiments to provide incompressible CFD validation data for a rectangular, constant-area duct with S-ducts upstream and downstream. The Reynolds numbers tested, based on hydraulic diameter, were 790 and 40,000.

Received Oct. 15, 1991; revision received July 13, 1992; accepted for publication Oct. 30, 1992.

*Senior Staff Scientist, Lewis Research Center Group. Associate Fellow AIAA.
†Supervisor, Lewis Research Center Group. Member AIAA.
‡Research Engineer, Lewis Research Center Group. Member AIAA.

Numerical

Rowe[6] provided early experiments and inviscid computations of flow in a 45 deg-45 deg S-bend and a 180-deg pipe, with Reynolds number of 2.36×10^5, based on diameter. Towne and Anderson[7] conducted a numerical study with a PNS computer program of a circular S-duct for incompressible flow with a diameter-based Reynolds number of 2000. They also analyzed the F-16 inlet duct with an elliptical inlet and a round exit. A turbulent flow calculation was completed with a Reynolds number of 1.44×10^7 and an entrance Mach number of 0.9 with the inlet flowfield specified. Good agreement with exit total pressure data was obtained. Vakili et al.[8,9] reported experimental and computational (parabolic Navier-Stokes) results for a 30 deg-30 deg nondiffusing S-duct, which is also the nondiffusing duct analyzed in this article. (The present study reports solutions of the full Navier-Stokes equations.) The inlet Mach number was 0.6, and the Reynolds number was 3.25×10^6/ft. The PNS computation agreed well with the experimental total pressures and velocity vectors. Towne[10] used a PNS code to predict the total pressure field for several Royal Aeronautical Establishment (RAE) inlet ducts with offsets of 0.3 and 0.45, and with and without centerbody hubs. Predicted total pressure profiles were in good agreement with experiment results.

Malechi and Lord[11] used a PNS code to calculate the flowfield of two circular-to-rectangular transition ducts. These ducts produced a pair of counter-rotating vortices like those of S-ducts. The authors concluded that it was important to have accurate inlet boundary-layer profiles to calculate accurately the (fixed) input static-pressure field necessary for the PNS solution. The PNS solver underpredicted the vortex strength and the cross-sectional velocities. They used the k-ε turbulence model and concluded that the turbulent eddy viscosity was (numerically) suppressed in the vortex core. Cosner[12] reported a FNS simulation of a compact, highly offset diffuser with an inlet Mach number of 0.777. The boundary-layer separated from the inner bend of the diffuser at half the diffuser length. Predictions were also made for a different diffuser with an assumed uniform inflow (with a boundary layer) at Mach 0.65.

Monson et al.[13,14] compared experimental data and FNS numerical results for a rectangular (Space Shuttle main engine) 180-deg U-duct. The Mach number was 0.1, and the Reynolds numbers, based on channel height, were 10^5 and 10^6. They concluded that simple mixing length models are inadequate for strong secondary flows.

Jenkins and Loeffler[15] compared thin layer Navier-Stokes results with data for a diffusing S-duct with an inlet Mach number of 0.34 and Reynolds number of 5.75×10^5. Results were obtained using the Baldwin-Lomax turbulence model and a one-half equation turbulence model. The authors conclude that the major flow features were well simulated, except in the separated region, where the predicted pressures did not agree with experimental values, and that more complex turbulence models are needed.

Conclusions from the Literature

Vortex pairs are evident in the exit planes of S-ducts, transition ducts, and bending rectangular ducts. These vortices are due to secondary flows induced by pressure gradients. However, although bench mark CFD validation data exist for incompressible flow, few data sets are available for compressible CFD validation. Thus, additional experimental data are needed for code validation of flow with strong crossflow. A possible limitation of both algebraic and k-ε turbulence modeling for strong secondary flows has been noted by several researchers.

The mechanism that produces the low total pressure region at the exit is an inviscid rotational phenomenon, provided an inlet boundary layer is present. Therefore, correct inlet boundary conditions are obviously needed. Previous computational investigations appear to be limited to FNS or PNS computations that do not account for the upstream effect of mass flow adjustment, boundary-layer growth, and flow blockage; i.e., the published solutions have specified inlet conditions, with the exception of Ref. 15. In this present study, the upstream static conditions were allowed to adjust (total conditions were constant), and the inviscid contributions to the secondary flowfield were examined.

Experiment Description

In the present study the experiments of Vakili et al.[8,9,16] are modeled. The nondiffusing S-duct[8,9] had a circular constant-area cross section with two 30-deg bends (Fig. 1). A 29.9-in. straight pipe was connected to a plenum to provide uniform flow and fully developed turbulent boundary layers to the S-duct. The inlet boundary layer was turbulent and was 7.8% of the 3.25-in. duct inside radius. The average inlet Mach number was 0.6. The radius of curvature, R, of 33 in. was about 5 diam. A 65-in. straight section was installed behind the S-duct, and the flow exited to ambient air. The Reynolds number was 1.76×10^6 based on upstream duct diameter. The diffusing duct[16] is similar in installation, and the area ratio of the duct exit to inlet is 1.51. The offset of the S-duct is approximately 1.5 upstream duct diameters.

Wall static pressures were measured along three azimuth angles of 0 deg (top), 90 and 180 deg (bottom), for the nondiffusing duct and of 10, 90, and 170 deg for the diffusing duct. Total pressure profiles were measured at six axial locations, including a reference station. Velocity and static pressure fields were also measured.

Analysis Computer Program

The PARC3D[17] computer program solves the full, three-dimensional Reynolds-averaged Navier-Stokes equations in strong conservation form with the Beam and Warming approximate factorization algorithm. The implicit scheme uses central differencing for a curvilinear set of coordinates. The code was originally developed as AIR3D by Pulliam and Steger[18]; Pulliam later added the Jameson[19] artificial dissipation and called the code ARC3D.[20] Cooper adapted the ARC3D code for internal propulsion application and named the code PARC3D.

Turbulence Model

The Baldwin-Lomax[21] algebraic turbulence model, developed for two-dimensional flow, assumes isotropic equilibrium turbulence and has no allowance for secondary flow effects. The wall weighting logic for the H-grid uses the smaller of the two values of eddy viscosity calculated at a point due to each "wall." The logic for the O-grid uses only one value of eddy viscosity at each radial and angular position.

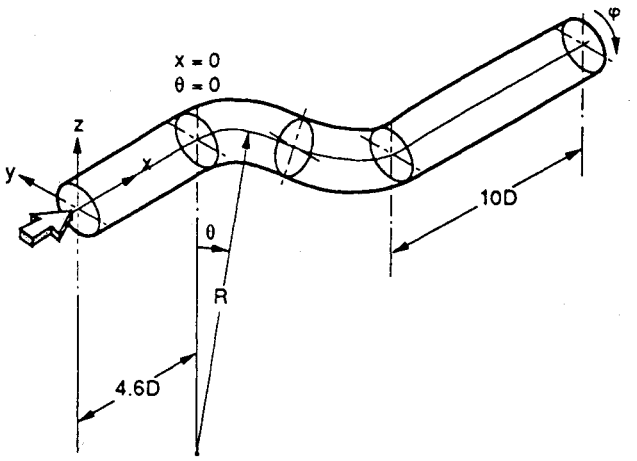

Fig. 1 Geometry of nondiffusing S-duct.

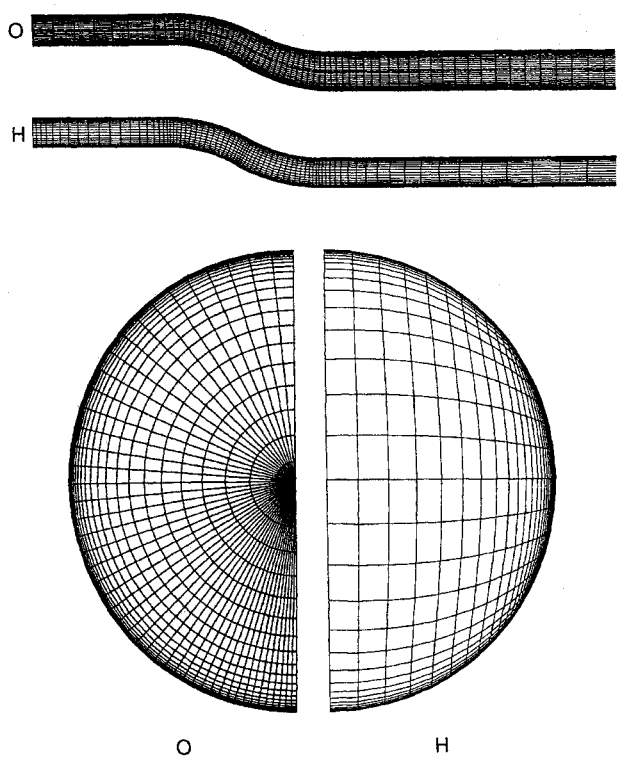

Fig. 2 Grid geometries for H-grid (nondiffusing duct shown) and O-grid (diffusing duct shown).

Grid

When analyzing flows in realistic ducts, the cross-sectional shape often changes from rectangular to circular or vice versa. Therefore, one type of grid may not fit the boundaries throughout the duct. An H-grid conforms well to a rectangular cross section, and an O-grid conforms well to a circular cross section. One feature of the O-grid "pole" boundary condition is that the center boundary condition is an average of the surrounding flow properties. The H-grid may not conform well to curved boundaries, and the "corner points" of the grid can cause excessive grid skewness (nonorthogonal grids). In this study, the effects on the numerical solutions using both a H-grid and a O-grid (Fig. 2) are investigated to provide insight into numerical effects. For the nondiffusing S-duct, the H-grid dimensions are 75 × 33 × 33 and 75 × 35 × 31 for the O-grid in the streamwise, circumferential, and radial directions, respectively. For the diffusing S-duct, the H-grid dimensions are 75 × 33 × 33 and the O-grid dimensions are 65 × 49 × 26. The H-grids were generated with the INGRID3D[22] code, which uses algebraic equations and an elliptic solver to smooth the H-grids. The grid was considered practical even though the computer memory limits and run times were taxed. The software used to refine the H-grid could not further decrease the radial spacing because of skewness problems. The run times were on the order of 25 Cray hours for each of the two solutions. Additional grid refinement could be done with an attendant increase in resources.

Boundary Conditions

The boundary conditions used were no-slip at the adiabatic walls, slip on the symmetry plane, zero normal static pressure gradients, total pressure, and temperature specified at the entry plane. At the exit plane the static pressure is specified and the other flow variables are extrapolated. The entrance velocity and static pressure were solved by averaging an incoming and an extrapolated interior Riemann invariant.

Numerical Issues

The norm of the residuals was dropped by over three orders of magnitude. Mass was conserved within 1% at each axial station. About 30 Cray XMP hours were used for the diffusing S-duct and 20 for the nondiffusing S-duct.

Results and Discussion

Nondiffusing S-Duct Computational Results

Fully Viscous Solution

The surface static-pressure distributions obtained from the H- and O-grid solutions are similar. Both solutions agree reasonably well with the test data. Figure 3 shows the O-grid results compared with the measured distribution. The six measurement stations, including the reference station, are indicated in Fig. 3. The predicted pressures are nearly linear with S/D along the 90-deg angular position; whereas the experimental data are higher than the predicted values along this line.

Total Pressures

Agreement in total pressure is very good between the O-grid solution and the experimental total pressure contours at station VI (Fig. 4). The total pressure coefficient is $(p_{t,\text{local}} - p_{s,\text{ref}})/q_{\text{ref}}$. The results obtained with the H-grid are similar. Analysis of the computed flowfield indicates that the secondary flow develops very rapidly in the second bend. This is due to the change in the static-pressure gradient, which reinforces the secondary flow development in the second bend. In the first bend (Fig. 3) the higher static pressure is at the outer region of the duct, which tends to retard fluid motion near the wall. In the second bend, the higher static pressure is again at the outer region of the duct, which now tends to push the flow away from the walls.

The computed total-pressure field at station VI (Fig. 4) indicates that the computed secondary flow is not as strong as in the experiment. This discrepancy may be due to secondary flow and vorticity effects not being properly accounted for in the turbulence modeling. Another possible cause for the discrepancy is that the boundary-layer resolution may be inadequate. The Y^+ distance of the first grid point off the wall is approximately 19 for the O-grid and is located in the buffer region of the boundary layer. The vorticity generation and convection in the boundary layer are also affected by the secondary flow.

Boundary Layers

Predicted boundary-layer thickness is plotted vs distance in Fig. 5 for the O-grid. (The H-grid provided similar results.[23]) The boundary-layer thickness is defined as the perpendicular distance from the wall, where the total-pressure coefficient is 1.025. At this value of C_{pt} the velocity is 0.99 of freestream. Flat plate boundary-layer thickness is shown for comparison. The boundary layers on the 180-deg (bottom) surface grow fastest because of the accumulation of boundary layer before the first bend, and because of the strengthening of the vortex

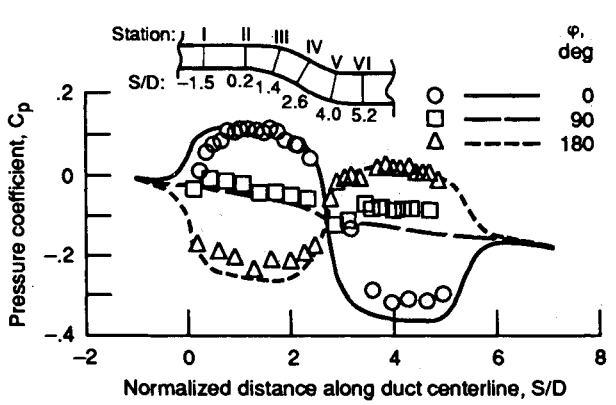

Fig. 3 Nondiffusing S-duct surface static pressure distributions with viscous flow for O-grid.

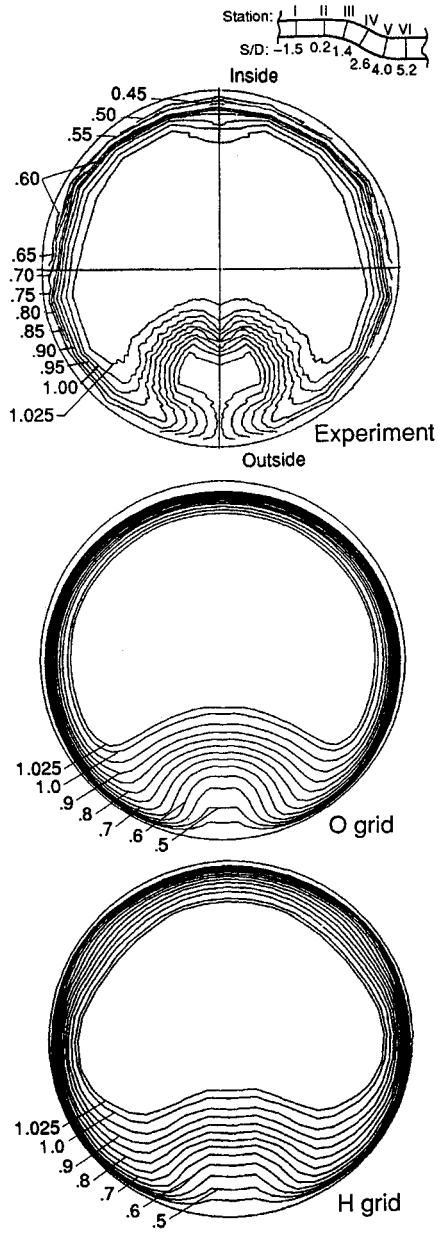

Fig. 4 Nondiffusing S-duct contours of total pressure at station VI.

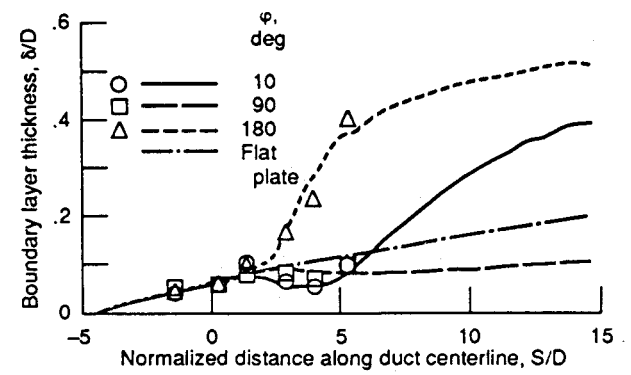

Fig. 5 Nondiffusing S-duct boundary-layer growth as computed using O-grid and H-grid.

aft of the first bend. The boundary layer along the 0-deg (top) surface grows at the next highest rate, and the boundary-layer along the 90-deg (side) surface grows more like that of a flat plate. The boundary-layer thickness increases rapidly along the 180-deg (bottom) surface at an S/D of approximately 2. The computed reference station velocity profiles are similar to the $\frac{1}{7}$ power law for both grids.[23]

The O-grid velocity profiles are shown in Fig. 6 for the reference station and stations IV and VI. The experimental data are also shown in the figure. The friction velocity used to normalize both the computational and the experimental results was obtained by a successive substitution procedure, which fits one of the computational points to the law of the wall. The first experimental data point was quite high in the boundary layer (Y^+ of about 1000) and was assumed to be in the linear region. This assumption was made for both the computational and experimental profiles because the first points were not in the linear sublayer. The computed C_f distributions are given in Ref. 23.

Diffusing S-Duct Computational Results

Static Pressure

The surface static pressure distributions obtained from the O- and H-grid solutions are compared with the measured distribution in Fig. 7. The H-grid solution provides better agreement with the experimental data downstream of the separation than the O-grid results. This result may be a result of better grid packing in the separation zone (Fig. 2), or of the logic used in the turbulence length scale search (previously mentioned in the Turbulence Model section). The location of

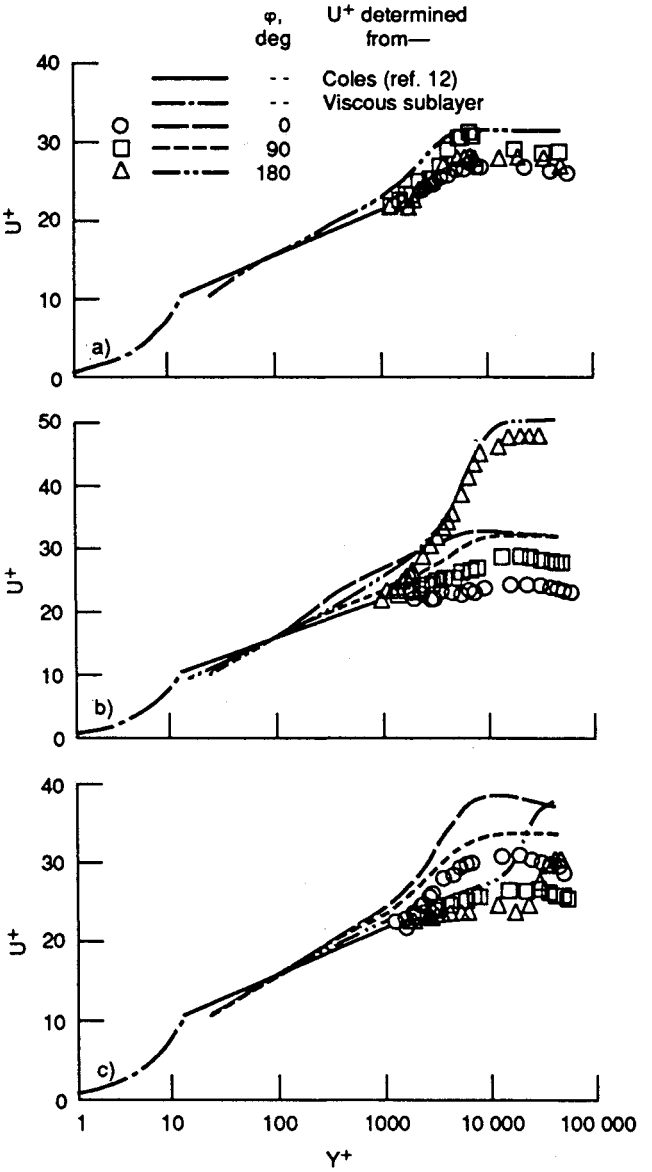

Fig. 6 U^+ vs Y^+ for nondiffusing duct, O-grid for a) reference station, b) station IV, and c) station VI.

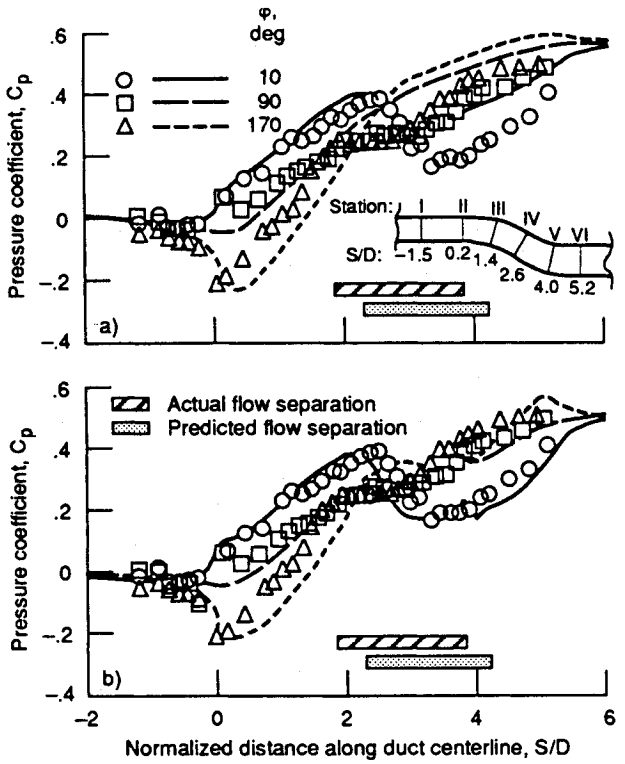

Fig. 7 Diffusing S-duct surface static pressure distribution, viscous flow for a) O-grid and b) H-grid.

the separation bubble for both solutions was approximately one-half duct diameter downstream of the experimental separation point. Recall that the surface static pressures predicted in a nondiffusing, nonseparating S-duct (Fig. 3) were in good agreement with the data. The inaccurate prediction of flow separation leads to inaccurate prediction of static pressures in the separating duct flow case because of aerodynamic area changes.

Total Pressures

Computational and experimental total pressure contours at station VI are compared in Fig. 8. Agreement is reasonable between the O-grid solution and the experimental contours. The H-grid provided similar results. The computed results at station VI indicate that the computed secondary flow is not as strong as the experimental, since the predicted region of "inviscid" core flow is larger than the measured region. This discrepancy may be due to boundary-layer resolution and/or turbulence modeling. The Y^+ distance of the first grid point off the wall is approximately 10, which is in the buffer layer. Another possible contributing factor is that the turbulence model may be predicting too much eddy viscosity in the vortex region and is damping the vortex development.

Boundary Layers

The variations of boundary-layer thickness at angular positions from the top of the duct, ϕ, of 0, 90, and 180 deg as a function of duct length are shown in Fig. 9 for the O-grid solution. The corresponding growth of a boundary layer along a flat plate, with no pressure gradient, is also shown. The most significant departure from the growth along a flat plate is for ϕ = 180 deg, which contains the separated region and the secondary flow vortices. The data indicate a more rapid boundary-layer growth near the duct exit (S/D = 5) than the computations indicate. The measured boundary-layer growth follows the growth along the flat plate at the other two locations.

The O-grid velocity profiles, in wall coordinates, are shown in Fig. 10 for the reference station and stations IV and VI.

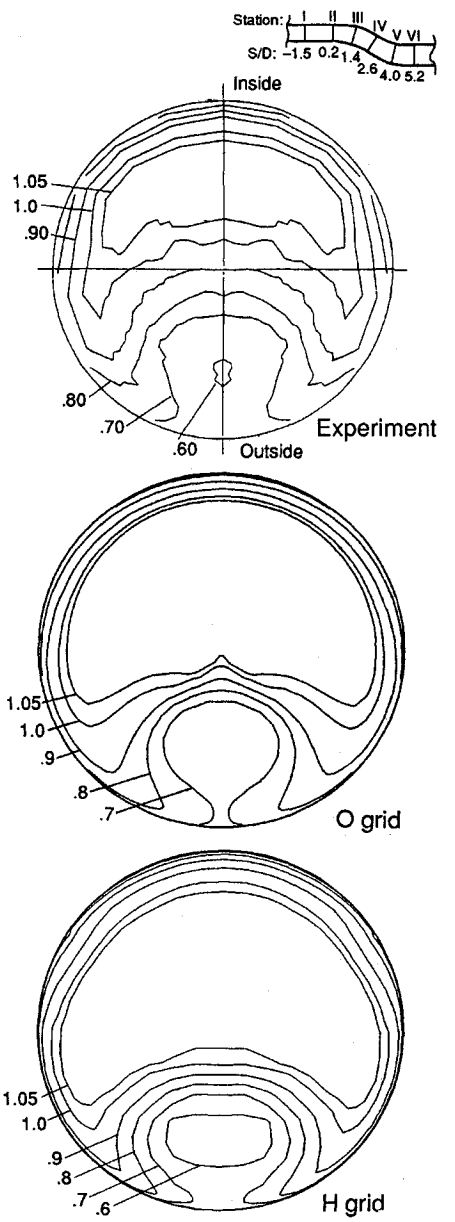

Fig. 8 Diffusing S-duct contours of total pressure; viscous flow; station VI.

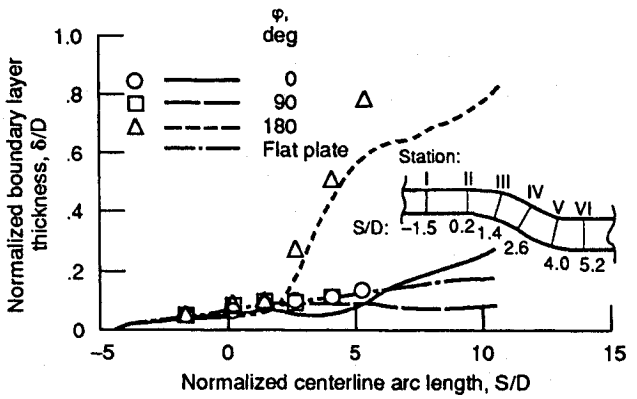

Fig. 9 Diffusing S-duct boundary-layer development; O-grid.

At the reference station, the predicted velocity profile agrees well with the law of the wall. At station IV the flow is separated, and the boundary layer in this region, at ϕ = 170 deg, departs significantly from this law. This phenomena is also noted in the work reported by Schubauer and Klebanoff[24] and Baldwin-Lomax.[21] At station VI the flow is reattached, and a large vortical flow is present, which causes the bound-

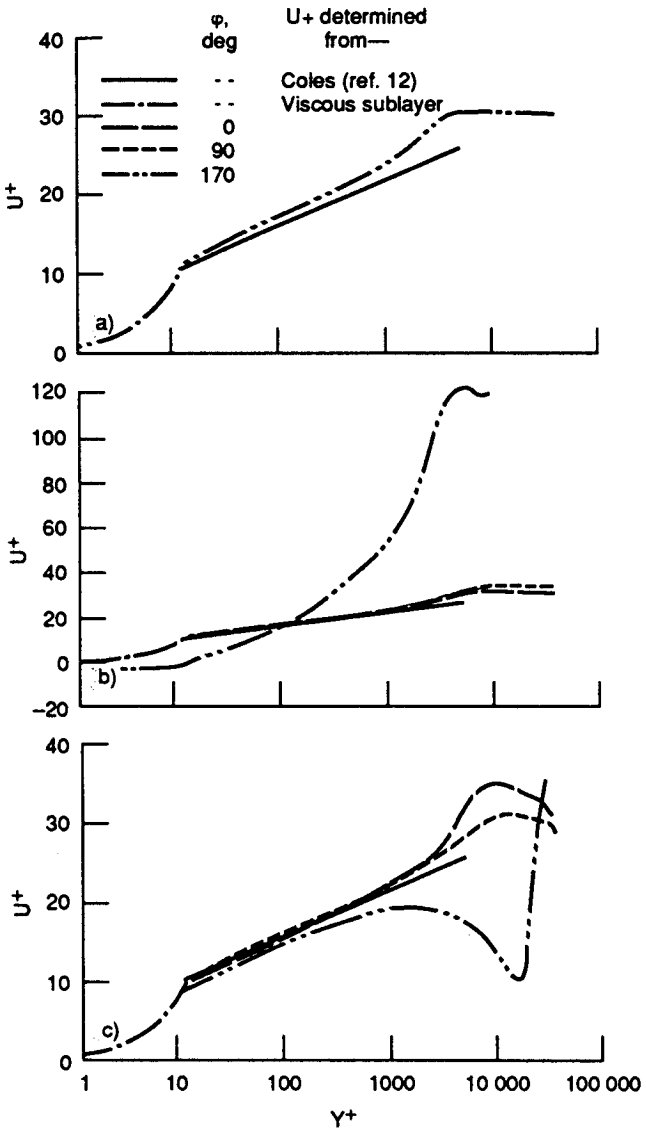

Fig. 10 Diffusing S-duct U^+ vs Y^+ at stations a) I, b) IV, and c) VI; O-grid.

ary-layer profile to deviate from the law of the wall for ϕ = 170 deg. The skin friction coefficients, obtained from the O-grid solution, are plotted as a function of axial distance for ϕ = 10, 90, and 170 deg in Fig. 11.

Flow Separation

The predicted H-grid streamlines in the region of flow separation are compared with the paint flow visualization in Fig. 12. The predicted flowfield is in general agreement with the data. The O-grid streamlines are similar to those of the H-grid. As previously mentioned, the predicted location of the separation for both grids is approximately one-half duct diameter downstream of the actual point of separation. This poor prediction of the separation location is thought to be partly due to the simple turbulence model used, which was developed for two-dimensional, mildly separated flow. In this case, however, the flow is three-dimensional, with a very strong secondary flow present. Such a complex flow may be beyond the capabilities of this turbulence model to handle correctly. Alternatively, increased grid resolution in this region of flow separation may improve the computed results.

Discussion for Both S-Ducts

Euler Solutions with Irrotational and Rotational Inflow

To investigate the inviscid contributions to the secondary flow and examine the magnitude of the viscous effects, the

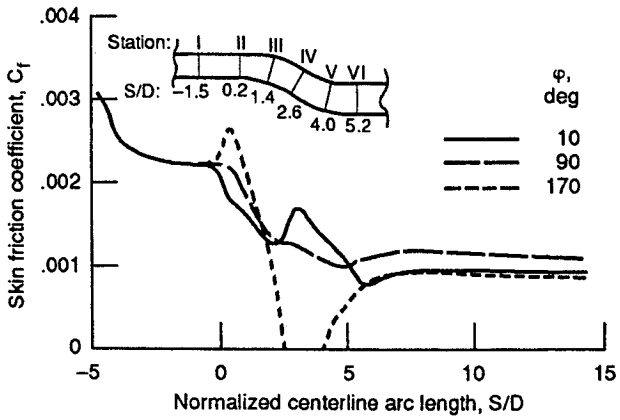

Fig. 11 Diffusing S-duct coefficient of friction vs *S/D*; O-grid.

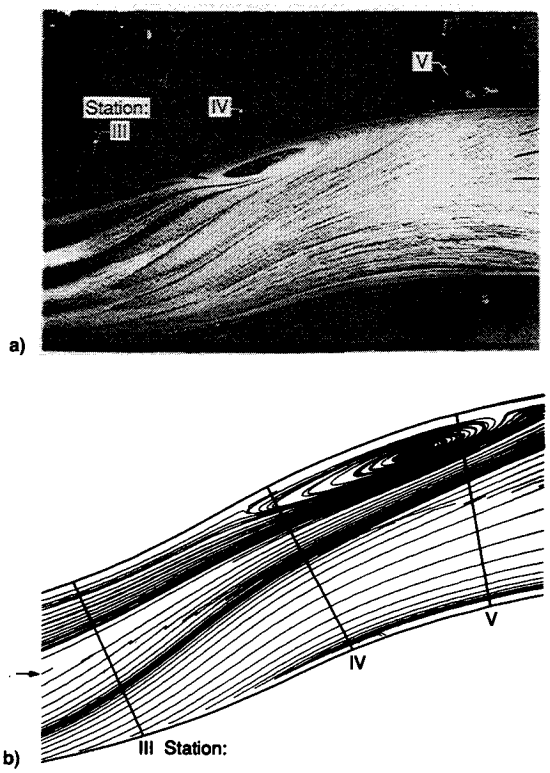

Fig. 12 Diffusing S-duct flow separation visualization: a) experiment, b) H-grid.

Euler equations were solved for irrotational and rotational inflow conditions using an O-grid. For both the irrotational and rotational flow cases, the downstream pressure was adjusted to obtain the same mass flow. A uniform inflow was used for the irrotational flow case. For the rotational flow case, the inflow was held fixed using the fully viscous calculations discussed below, and the interior flow was considered inviscid.

Vorticity Contours

Classical theories by Squire and Winter[26] attribute the origin of secondary flows to the streamwise deflection of the transverse vorticity component in the incoming (upstream) boundary layer. Vortex stretching results in the generation of counter-rotating vortices. The computed irrotational flow results,[23,25] showed no secondary flow development, which is consistent with these theories. Contours of streamwise vorticity for the nondiffusing and diffusing S-ducts at station VI are reported in Refs. 23 and 25 for both the inviscid rotational flow and for fully turbulent flow. The inviscid rotational flow accounts for a significant portion of the secondary flow present in the fully viscous case.

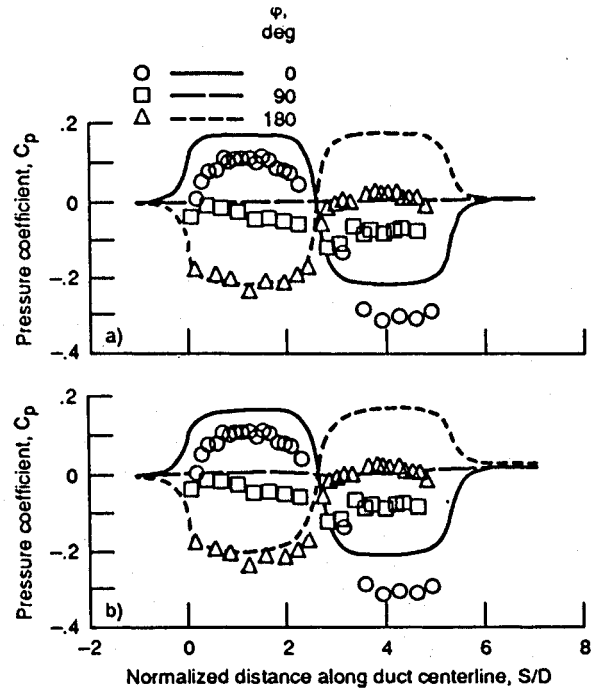

Fig. 13 Nondiffusing S-duct surface static pressure distribution, O-grid: a) irrotational flow, b) inviscid rotational flow.

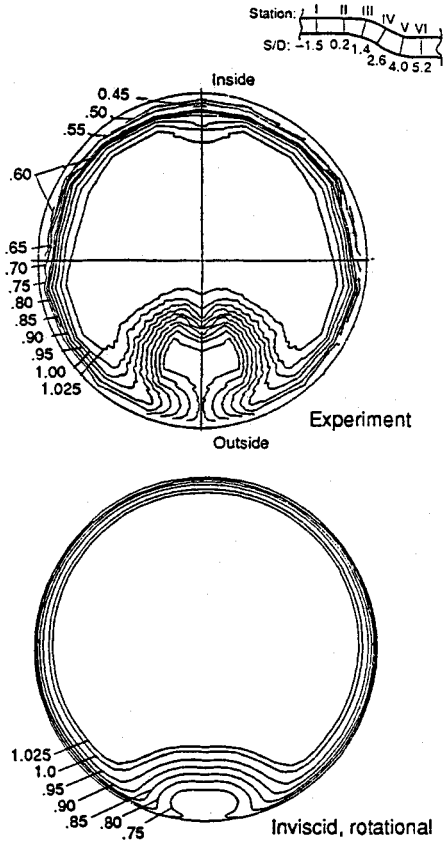

Fig. 14 Nondiffusing S-duct total pressure contours for inviscid rotational flow; station VI; O-grid.

Nondiffusing S-Duct

The computed surface static pressures for the irrotational and rotational flow cases are shown in Fig. 13 using the O-grid results. The general shapes of these profiles are similar to each other, which implies that the streamwise pressure gradients are determined primarily by irrotational effects. The experimental pressures should not, and do not, agree with the computations, because there are no pressure losses in either of these two approximations. The total pressure contours at station VI (Fig. 14) can be directly compared with the fully viscous results shown in Fig. 4. The two counter-rotating vortices are evident in Fig. 14. The vortex strength is, however, significantly weaker than that of the experiment. The secondary flow is driven by the inviscid pressure field; however, the turbulent eddy viscosity generation affects the strength of the secondary flow. The effects of the inlet vorticity on the total pressure and secondary flowfields are reflected in Fig. 14.

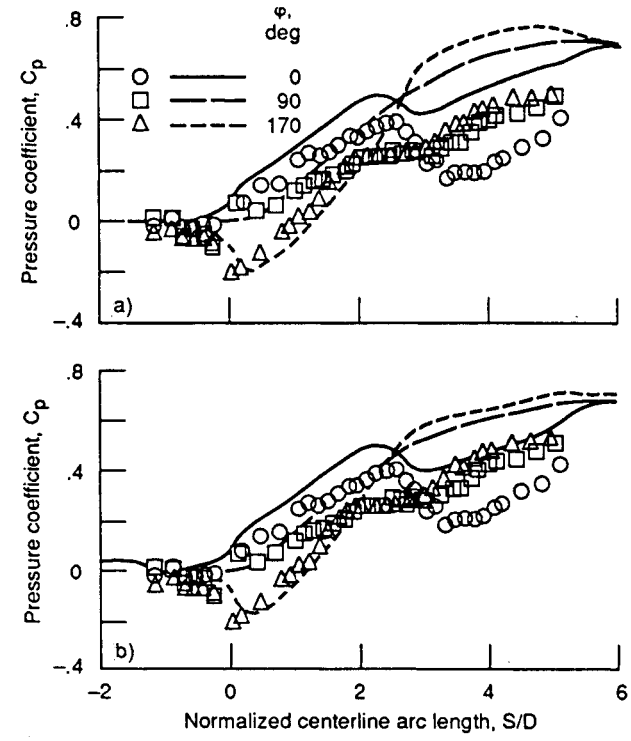

Fig. 15 Diffusing S-duct surface static pressure distribution, O-grid: a) irrotational flow, b) inviscid rotational flow.

Diffusing S-Duct

The computed surface static pressures for the irrotational and rotational flow cases are shown in Fig. 15. As for the nondiffusing case, the general shapes of these profiles are similar to each other and to the experimental data. Their similarity implies that the streamwise pressure gradients are determined primarily by irrotational effects. Of course, the actual pressures are influenced by the rotational and viscous effects.

Concluding Remarks

The computed total pressures are generally in good agreement with the experimental data. Both the H- and the O-grids provided similar results, with the O-grid providing smoother turbulent eddy viscosities due to the lack of the "corner effects." The predicted static pressures do not compare as well with the measurements, possibly due to a failure of the turbulence model to properly account for secondary flow and imbedded vorticity effects, or possibly because of undocumented disturbances in the inflow. However, the two counter-rotating vortices at the S-duct exit were predicted. The rotational Euler solutions show that the development of the secondary flows in S-ducts is driven by inviscid phenomena. Friction velocities were determined and used to obtain wall skin friction values.

The modeling could be improved by incorporating adaptive gridding and more advanced turbulence models. Grid refinement might improve the agreement between calculations and experiment, with the first grid point in the sublayer, e.g., Y^+

of 1–5. The complete duct length should be modeled because of the importance of vorticity generation effects. Additional fundamental experimental and numerical studies are necessary to properly address the turbulence modeling issues with imbedded vortices and strong secondary flows.

Acknowledgment

This work was prepared for NASA Lewis Research Center under Contract NAS3-25266, project monitor R. Coltrin.

References

[1]Bansod, P., and Bradshaw, P., "The Flow in S-Shaped Ducts," *Aeronautical Quarterly*, Vol. 23, No. 2, 1972, pp. 131–140.

[2]Willmer, A. C., Brown, T. W., and Goldsmith, E. L., "Effects of Intake Geometry on Circular Pitot Intake Performance at Zero and Low Forward Speeds," *Aerodynamics of Power Plant Installations*, AGARD, Paper 5, Neuilly-Sur-Seine, France, 1981, pp. 5-1–5-16.

[3]Guo, R. W., and Seddon, J., "An Investigation of the Swirl in an S-Duct," *Aeronautical Quarterly*, Vol. 33, No. 1, 1982, pp. 25–58.

[4]McMillan, O. J., "Mean-Flow Measurements of the Flow Field in a Diffusing Bend," NASA CR 3634, Nov. 1982.

[5]Schmidt, M. C., Whitelaw, J. H., and Yianneskis, M., "Flow in Out-of-Plane Double S-Bends," NASA CR-176981, June 1986.

[6]Rowe, M., "Measurements and Computations of Flow in a Pipe Bends," *Journal of Fluid Mechanics*, Vol. 43, Pt. 4, Oct. 2, 1970, pp. 771–783.

[7]Towne, C. E., and Anderson, B. H., "Numerical Simulation of Flows in Curved Diffusers with Cross-Sectional Transitioning Using a Three-Dimensional Viscous PNS Code," NASA TM-81672, Jan. 1981.

[8]Vakili, A., Wu, J. M., Hingst, W. R., and Towne, C. E., "Comparison of Experimental and Computational Compressible Flow in a S-Duct," AIAA Paper 84-0033, Jan. 1984.

[9]Vakili, A., Wu, J. M., Liver, P., and Bhat, M. K., "Measurements of Compressible Secondary Flows in a Circular S-Duct," AIAA Paper 83-1739, July 1983.

[10]Towne, C. E., and Flitcroft, J. E., "Analysis of Intake Ducts Using a Three-Dimensional Viscous Marching Procedure," First World Congress on Computational Mechanics, Austin, TX, Sept. 1986.

[11]Maleckl, R. E., and Lord, W. K., "Parabolized Navier-Stokes Analysis of Circular-to-Rectangular Transition Duct Flows," Society of Automotive Engineers Paper 881480, Oct. 1988.

[12]Cosner, R. R., "Transonic Propulsion System Integration Analysis at McDonnell Aircraft Company," *Transonic Symposium: Theory, Application, and Experiment*, NASA CP 3020, Vol. 1, Pt. 2, 1988, pp. 409–436.

[13]Monson, D. J., Seegmiller, H. L., and McConnaughey, P. K., "Comparison of LDV Measurements and Navier Stokes Solutions in a Two-Dimensional 180-Deg Turn-Around Duct," AIAA Paper 89-0275, Jan. 1989.

[14]Monson, D. J., personal communications, NASA Ames Research Center, Moffett Field, CA, Feb. 1990.

[15]Jenkins, R. C., and Loeffler, A. L., "Modeling of Subsonic Flow Through a Compact Offset Diffuser," *AIAA Journal*, Vol. 29, No. 3, 1991, pp. 401–408.

[16]Vakili, A., Wu, J. M., Liver, P., and Bhat, M. K., "Compressible Flow in a Diffusing S-Duct with Flow Separation," *Heat Transfer and Fluid Flow in Rotating Machinery*, edited by W. J. Yang, Hemisphere, 1987, pp. 201–211.

[17]Cooper, G. K., "The Parc Code: Theory and Usage," Arnold Engineering Development Center TR-87-24, Tullahoma, TN, Oct. 1987.

[18]Pulliam, T. H., and Steger, J. L., "Implicit Finite-Difference Simulations of Three-Dimensional Compressible Flow," *AIAA Journal*, Vol. 18, No. 2, 1980, pp. 159–167.

[19]Jameson, A., Schmidt, W., and Turkel, E., "Numerical Solutions of the Euler Equations by Finite Volume Methods Using Runge-Kutta Time-Stepping Schemes," AIAA Paper 81-1259, June 1981.

[20]Pulliam, T. H., "Euler and Thin Layer Navier-Stokes Codes: ARC2D, ARC3D," *Notes for Computational Fluid Dynamics User's Workshop*, Univ. of Tennessee Space Inst., UTSI Pub. E02-4005-023-84, Tullahoma, TN, 1984, pp. 15.1–15.85.

[21]Baldwin, B. S., and Lomax, H., "Thin Layer Approximation and Algebraic Model for Separated Turbulent Flows," AIAA Paper 78-257, Jan. 1978.

[22]Dorrell, E. W., and McClure, M. D., "3D Ingrid: Interactive Three-Dimensional Grid Generation," Arnold Engineering Development Center TR-87-40, Tullahoma, TN, April 1988.

[23]Harloff, G. J., DeBonis, J. R., Smith, C. F., and Bruns, J. E., "Three-Dimensional Turbulent Computations for a Nondiffusing S-Duct," NASA CR 4391, April 1992.

[24]Schubauer, G., and Klebanoff, P., "Investigation of Separation of the Turbulent Boundary Layer," NACA TN 2133, Aug. 1950.

[25]Smith, C. F., Bruns, J. E., Harloff, G. J., and DeBonis, J. R., "Three-Dimensional Turbulent Computations for a Diffusing S-Duct," NASA CR 4392, April 1992.

[26]Squire, H. B., and Winter, L. B., "The Secondary Flow in a Cascade of Airfoils in a Nonuniform Stream," *Journal of the Aeronautical Sciences*, Vol. 18, No. 4, 1951, pp. 271–277.